Supplementary Information

S1 Thermochemical parameterized evolution model

We modeled the thermo-chemical evolution of Mars' main envelopes: a fully molten, convecting metallic core of radius R_c, overlaid by a solid silicate envelope extending to the surface of the planet at the radius $r = R_p$, and surface temperature T_s. The viscosity within the silicate envelope, η, depends on temperature T and pressure P according to an Arrhenius relationship:

$$\eta(T,P) = \eta_0 \exp\left(\frac{E^* + PV^*}{R\,T} - \frac{E^* + P_{\rm ref}V^*}{R\,T_{\rm ref}}\right), \tag{1}$$

where E^* and V^* are the effective activation energy and activation volume (*i.e.*, the sensitivity of viscosity to temperature and pressure, respectively), R is the gas constant, $T_{\rm ref}$ and $P_{\rm ref}$ are the reference temperature and pressure at which viscosity equals the reference viscosity, η_0. The effective activation volume and energy can account for viscous deformation in the diffusion creep regime, or in the dislocation creep regime[1–3]. In the first case E^* and V^* correspond to the intrinsic values. In the latter case (diffusion creep), E^* and V^* correspond to the intrinsic diffusion creep values divided by the power law index, whose value is close to 3.5[4]. The strong sensitivity of viscosity to temperature and the relatively small size of Mars imply that its mantle convects in the stagnant lid regime. Consequently, we considered the presence of a time-evolving rigid lithospheric lid of thickness, D_l, overlying a convecting mantle. The lithospheric lid includes a crust of thickness $D_{\rm cr}$, density $\rho_{\rm cr}$, specific heat at constant pressure C_{cr}, and thermal conductivity $k_{\rm cr}$, enriched in heat-producing elements. Our modeling approach follows closely the one described in previous works[5–7], which

we describe below for the sake of completeness.

The approach consists in solving a set of coupled ordinary differential equations that describe heat exchange between different domains. These are the energy balance for the convecting mantle and the core written below:

$$\rho_m C_m V_m \epsilon_m (St+1) \frac{dT_m}{dt} = -\left\{ q_m + \rho_{cr} \frac{dD_{cr}}{dt} [L_m + C_{cr}(T_m - T_l)] \right\} A_m + q_c A_c + H_m V_m, \tag{2}$$

$$\rho_c C_c V_c \epsilon_c \frac{dT_c}{dt} = -q_c A_c, \tag{3}$$

where t is the time, T_m is the mantle temperature at the top of the convecting mantle, and T_c is the temperature at the core-mantle boundary. ρ_m and ρ_c are the mantle and the core densities. C_m and C_c are mantle and core specific heat at constant pressure, A_m and A_c are the surface of the convecting mantle and core. V_m is the volume of the convective mantle, V_c is the volume of the core, and H_m is the volumetric internal heating rate due to the presence of heat-producing elements. L_m is the latent heat of silicates melting. ϵ_m expresses the ratio between the convecting mantle temperature and T_m and is constantly updated, while ϵ_c is the ratio between the average core temperature and T_c and set to 1.05. T_l is the temperature at the base of the stagnant lid. The latter is defined as the temperature at which viscosity has grown by one order of magnitude with respect to the convecting mantle, yielding[8]:

$$T_l = T_m - a_{\mathrm{rh}} \frac{R\, T_m^2}{E^*} \ , \tag{4}$$

in which $a_{\mathrm{rh}} = 2.54$ chosen based on the comparison between parameterized and 3D spherical modeling[9].

The heat flow out of the surface of the convecting mantle, q_m, is:

$$q_m = k_m \frac{T_m - T_l}{\delta_u}, \tag{5}$$

where k_m is the mantle thermal conductivity, δ_u is the thickness of the upper thermal boundary layer of the convecting mantle.

Similarly to Eq. (5) , the heat flow out of the core and into the mantle is:

$$q_c = k_m \frac{T_c - T_b}{\delta_c}, \tag{6}$$

where T_b is the temperature at the base of the convecting mantle. The latter is expressed by adding the contribution of the adiabatic gradient to T_m, namely:

$$T_b = T_m + \frac{\alpha_m g T_m}{C_m} \Delta R, \tag{7}$$

where α_m is the silicates thermal expansion coefficient, g is the surface gravitational acceleration, and $\Delta R = R_p - D_l - R_c - \delta u - \delta c$ is the thickness of the convecting mantle devoid of its thermal boundary layers.

The thickness of the upper thermal boundary layer is derived from boundary layer theory:

$$\delta_u = (R_l - R_c) \left(\frac{Ra_c}{Ra} \right)^{\beta_u}, \tag{8}$$

where $\beta_u = 0.335$ (together with the value of $a_{\rm rh} = 2.54$ in equation (4)) allows for the closest match between parameterized and 3D spherical modeling of stagnant lid convection with variable viscosity[9]. The thermal Rayleigh number associated with the convecting mantle is defined as:

$$Ra = \frac{\rho_m \alpha_m g \Delta T (R_p - D_l - R_c)^3}{\eta_m \kappa_m}, \tag{9}$$

which expresses the mantle convective vigor. In the definition above, $\kappa_m =$

$k_m/(\rho_m C_m)$ is the mantle thermal diffusivity, $\eta_m = \eta(T_m, P_m)$ is the viscosity of the mantle below the stagnant lid, and $\Delta T = T_m - T_l + T_c - T_b$ is the temperature difference across the upper and lower thermal boundary layers of the convecting mantle. $Ra_c = 450$ is the critical Rayleigh number. Note that when $Ra < Ra_c$, q_m and δ_u are set to 0.

Similarly, the thickness of the lower thermal boundary layer is:

$$\delta_b = \left(\frac{\kappa_m \eta_c Rai_c}{\rho_m \alpha_m g |T_c - T_b|} \right)^{1/3}, \tag{10}$$

where $\eta_c = \eta((T_b + T_c)/2), P_c)$ is the mantle viscosity taken at temperature and pressure half-way across the lower thermal boundary layer. $Ra_{i,cr}$ is the local critical Rayleigh number given by[10]:

$$Rai_c = 0.28\ Ra_i^{0.21}, \tag{11}$$

where Ra_i is the thermal Rayleigh number for the entire mantle:

$$Ra_i = \frac{\rho_m \alpha_m g \Delta T_i (R_p - R_c)^3}{\eta_m \kappa_m}, \tag{12}$$

and $\Delta T_i = (T_m - T_s) + (T_c - T_b)$ is the sum of the temperature contrasts across the entire rigid lid (including the mobile upper thermal boundary layer), and the basal thermal boundary layer.

The model accounts for crustal formation, in which latent heat is consumed or released upon melting and crystallization at shallow depths, through the use of a time-dependent Stefan number:

$$St = \frac{L_m V_a}{C_m V_m} \frac{dm_a}{dT_m}, \tag{13}$$

where V_a is the volume of the melt zone, and m_a is the volume-averaged melt

fraction ϕ:

$$m_a = \frac{1}{V_a}\int_{V_a}\frac{T(r)-T_{\rm sol}}{T_{\rm liq}-T_{\rm sol}}dV = \frac{1}{V_a}\int_{V_a}\phi(r)dV, \tag{14}$$

in which the solidus liquidus parametrization $T_{\rm sol\ peridotite} = 1409 + 134.2P - 6.581P^2 + 0.1054P^3$ and $T_{\rm liq} = 2035 + 57.46P - 3.487P^2 + 0.0769P^3$ (with P expressed in GPa) for dry peridotite were considered[11]. Melting above pressures of 7.4 GPa is not considered for crust formation because melt becomes denser beyond this limit[12]. In Eq. (14) , the solidus is shifted by adding a term that accounts for the increase in refractoriness of the residual mantle[6]:

$$T_{\rm sol} = T_{\rm sol\ peridotite} + \Delta T_{sol}\frac{D_{cr}}{D_{\rm ref}}, \tag{15}$$

where $D_{\rm ref}$ represents a reference crustal thickness that yields a solidus increase of ΔT_{sol} upon a 20% melt extraction of the total silicate volume:

$$D_{\rm ref} = \frac{0.2}{3}\frac{R_p^3 - R_c^3}{R_p^2}, \tag{16}$$

ΔT_{sol} specifies the total maximum solidus change occurring upon melt extraction. The crustal growth rate is then computed as[6]:

$$\frac{dD_{cr}}{dt} = u\ m_a\frac{V_a}{4\pi R_p^3}, \tag{17}$$

where u is the magnitude of mantle convective velocity:

$$u = u_0\left(\frac{Ra}{Ra_c}\right)^{2/3}, \tag{18}$$

and u_0 is the convective velocity scale.

Deep mantle melting that does not contribute to crustal production is also taken into account, as it directly affects heat balance through the latent cooling

and heating, as well as indirectly through possibly sharp and large changes in mantle viscosity[13]. Therefore, below the depth corresponding to $P > 7.4$ GPa we compute the melt fraction within the mantle $\phi(r) = (T_{\rm sol} - T)/(T_{\rm liq} - T_{\rm sol})$. Then, mantle viscosity is altered by the presence of melt as follows:

$$\eta(T, P, \bar{\phi} > 0) = \frac{\eta(T,P)}{2}\left[1 + \tanh\left(\frac{\phi_c}{w_m} - \bar{\phi}\right)\right] + \eta_{\rm liq}, \tag{19}$$

where $\bar{\phi}$ is the volume-averaged melt fraction in the deep mantle, $\eta_{\rm liq}$ is the viscosity of liquid peridotite set to 1 Pa s[14]. The quantities, ϕ_c and w_m express the sensitivity of mantle viscosity to melt fraction, and the width over which the viscosity jump occurs due to the presence of melt, respectively. We set $\phi_c = 0.1$ (*i.e.*, viscosity is sensitive small melt fractions) and $w_m = 0.1$ (*i.e.*, viscosity drop due to the presence of melt is relatively sharp). Other parameterizations were tested (*e.g.*,[15,16]) but did not yield significant differences because they all lead to relatively sharp decrease in viscosity for small amounts of melt. Therefore, we used the above simple expression, which retains these characteristics, and whose continuity yields good numerical stability. Upon deep melting production, the Stefan number defined in Eq. (13) is modified as $St = \frac{L_m V_{\rm melt}}{C_m V_m}\frac{dm_{\rm melt}}{dT_m}$, where $V_{\rm melt}$ and $m_{\rm melt}$ refers to the total volume and mass of mantle melting.

The time-dependent lid thickness, D_l, is obtained by solving the energy balance at its base:

$$\rho_m C_m (T_m - T_l)\frac{dD_l}{dt} = -\left\{q_m - \rho_{cr}\left[L_m + C_m(T_m - T_s)\right]\frac{dD_{cr}}{dt}\right\} + k_m \frac{\partial T}{\partial r}|_{r=R_l}. \tag{20}$$

The temperature gradient at the base of the lid (last term on the right-hand side of the equation above) is determined by solving the time-dependent

diffusion equation within the conductive lid:

$$\rho(r)C(r)\frac{\partial T}{\partial t} = \frac{1}{r^2}\frac{\partial}{\partial r}\left(r^2 k(r)\frac{\partial T}{\partial r}\right) + H(r), \tag{21}$$

where the density ρ, specific heat C, thermal conductivity k, and the volumetric internal heating rate, H, vary along the radius, r, and correspond to crustal values for $r > R_p - D_{cr}$, or mantle values elsewhere. The above equation is discretized with an implicit finite-difference scheme, in which the lithosphere is discretized using a regular grid. Since the lithosphere thickness evolves, the grid is re-meshed at each time step. The lithospheric temperature profile from the previous time step is constantly and linearly interpolated onto the new grid. This approach differs from one frequently used in such context, which involves the same grid with adaptative distortion through dynamical scaling of the radial coordinate[3,17]. Nevertheless, tests performed have shown that our numerical scheme yields essentially identical results (Fig. S2).

The partitioning of heat-producing elements between the mantle and the core is accounted for using a constant crustal enrichment factor, Λ, that expresses the ratio of crustal heat production rate to the heat production rate in the primitive mantle. Hence, the time-decaying mantle volumetric heating rate is:

$$H_m = \sum_i H_{0,i}\exp(-\lambda_i t)\left(1 + \frac{V_{cr}}{V_m}(1-\Lambda)\right) \tag{22}$$

where $H_{0,i}$ is the individual contribution of four heat-producing elements (^{238}U, ^{235}U, ^{232}Th, ^{40}K) at initial time $t = 0$, based on estimates from the concentration of incompatible elements in SNC meteorites[18], λ_i are the corresponding radioactive decay constants, and V_{cr} is the volume of the crust.

By mass balance, the time-decaying crustal volumetric heating rate is:

$$H_{cr} = \sum_i H_{0,i} \exp(-\lambda_i t) \left(1 + \frac{V_{cr}}{V_m}\Lambda\right). \quad (23)$$

Table 1 and Table 2 summarize the meaning and the values of the main physical quantities involved in the thermo-chemical modeling described above.

The parameterized evolution model described above allows a large parameter space to be explored at a reasonable computational cost. For the purpose of our study, the parameter space exploration requires several hundreds of thousands of evolutions to be computed (section S5 and Table 2). Under such circumstances, the use of spherical convection models[1] would be computationally prohibitive.

Previous studies have reported a good match between parameterized planetary evolution models and fully dynamic models, including cases where a convective asymmetry develops between the upper and lower thermal boundaries[1,9,19]. This is notably the case for Mars in spherical geometry where viscosity is temperature and pressure-dependent[1,9,20].

We compared our parameterized model described above with the results from a fully dynamic mantle evolution model in spherical geometry from *Thiriet et al.*[9]. This corresponds the to case name "*Mars1*" in the Table 3 of their paper, whose evolution is displayed in their Figure 2. In particular, it has the following characteristics: E^*=300 kJ/mol, V^*=0 cm^3/mol, T_{m0} = 1750 K, T_{c0} = 2250 K, no crust, and Boussinesq approximation.

We used our parameterized model to reproduce this case. The results are displayed in Fig. S1a-c and compared with 3D results and the parameterized model of *Thiriet et al.*[9]. The results show that our parameterized model reproduces well the thermal evolution from spherical models, despite the asymmetry between the upper and lower thermal boundaries mainly due to the different temperatures in these regions. The latter leads to viscosity contrasts greater

than one order of magnitude between the upper and the CMB thermal boundary layers. The obtained surface and CMB heat flux evolutions (Fig. S1a-b) are very similar. The somewhat larger differences in lithospheric thicknesses (Fig. S1c) result primarily from the difficulty in defining the lithospheric thickness in spherical models. Indeed, if an alternative definition is used, the differences between parameterized and spherical models are further reduced[9]. In addition, the differences observed between the parameterized models of *Thiriet et al.*[9] and our implementation essentially result from the differences in initial lithospheric temperature profiles. While we assumed a linear profile for the initial lithospheric temperature, *Thiriet et al.*[9] used a profile based on the horizontally averaged temperature from the 3D model (M. Thiriet, personal communication). This difference in initial conditions slightly affects the evolutions.

To remove this bias we checked that when the initial conditions are identical, both our implementation and that of *Thiriet et al.* yield identical evolutions. This case is similar to the one described above, with the exception that V^*=6 cm^3/mol (*i.e.*, a temperature- and pressure-dependent mantle viscosity) and the initial lithospheric temperature profile is initialized using the same linear profile. The excellent agreement displayed in Fig. S2 validates our numerical implementation of the parameterized model equations.

Overall, these benchmarks validate our numerical implementation of the parameterized model equations, and show that our model reproduces well the evolutions computed in 3D spherical geometry.

S2 Orbital evolution model

We used the formalism of *FerrazMello, et al. 2008* [21] and *Heller, et al. [2011]*[22] to describe the orbital evolution of Phobos. The corresponding equations are those listed in section 2.2 of *Heller, et al. [2011]*[22], with several modifications.

Among them, we made the reasonable assumption of tidal locking in 1:1 spin orbit resonance, and neglect the influence of obliquities on the evolution of Phobos. In addition, since we consider a temperature and frequency-dependent tidal quality factor for Mars, we do not assume a constant phase lag, contrary to *Heller, et al. [2011]*[22]. Under these conditions, the orbital evolution of Phobos is governed by two coupled ordinary differential equations for the semi-major axis, a, and the orbital eccentricity, e:

$$\frac{da}{dt} = \frac{a^2\ Z'_p}{4GM_pM_s}\left[4\varepsilon'_0 + e^2\left(-20\varepsilon'_0 + \frac{147}{2}\varepsilon'_1 + \frac{1}{2}\varepsilon'_2 - 3\varepsilon'_5\right)\right] - \frac{21k_{2s}M_pnR_s^5e^2}{Q_sM_sa^4} \tag{24}$$

$$\frac{de}{dt} = \frac{-a\ e\ Z'_p}{8GM_pM_s}\left(2\varepsilon'_0 - \frac{49}{2}\varepsilon'_1 + \frac{1}{2}\varepsilon'_2 + 3\varepsilon'_5\right) - \frac{21}{2}\frac{k_{2s}M_pnR_s^5e}{Q_sM_sa^5}, \tag{25}$$

where G is the gravitational constant, M_p is the mass of Mars, M_s is the mass of Phobos, R_p is Mars radius, R_s is Phobos radius, $k_{2s} = 10^{-7}$ is Phobos Love number (assuming a monolith structure[23]), $Q_s = 100$[24] is Phobos tidal quality factor assumed to be constant, $n = \sqrt{G(M_p + M_s)/a^3}$ is the mean orbital motion, and ε'_0, ε'_1, ε'_2, ε'_5 express the contributions of different tidal waves at the following frequencies: $\omega_0 = 2\omega_p - 2n$, $\omega_1 = 2\omega_p - 3n$, $\omega_2 = 2\omega_p - n$, $\omega_5 = n$, respectively, where ω_p is Mars' rotational frequency assumed to be constant. These contributions are given by:

$$\varepsilon'_{i=0,1,3,5} = sign(\omega_i)\left(\frac{|\omega_i|}{\omega}\right)^{-\alpha_q}, \tag{26}$$

where α_q is the power law slope that expresses the frequency dependence of tidal dissipation (described in the next section, see Eq. (33)), the function $sign(X)$ returns the sign of X, or 0 if $X = 0$, and ω is the dominant tidal frequency, taken as the maximum between the annual (n) and semi-diurnal ($2|\omega_p - n|$)

frequencies. The above expressions therefore allows the frequency dependence of Mars' tidal dissipation for different tidal waves to be taken into account. Z'_p is given by:

$$Z'_p = \frac{k_2\,(1+f)}{Q}\,\frac{3G^2M_s^2(M_p+M_s)R_p^5}{\omega\ a^9}, \tag{27}$$

where Q is the time-dependent Mars' tidal quality factor taken at the dominant tidal frequency, whose calculation will be detailed in the next section.

On the right-hand side of Eq. (24) and Eq. (25) , the first terms refer to the contributions of Mars, while the second terms correspond to the contributions of Phobos.

The quantity $f = 2(k_3/k_2)(R_p/a)^2 + (10/3)(k_4/k_2)(R_p/a)^4$ absent in *Heller, et al. [2011]*[22] accounts for higher-order Love numbers, whose influence may be important for small semi-major axis values[25]. Since k_3 and k_4 are not known with good accuracy, we follow the approach of *Nimmo and Faul [2013]*[26], where the ratios k_3/k_2 and k_4/k_2 are assumed to be the same as those of the other Love numbers h_3/h_2 and h_4/h_2. Such ratios are better constrained within the ranges h_3/h_2 =0.39-0.69, and h_4/h_2=0.26-0.46[27] . While higher-end values of these ratios (resulting in larger f) values could be used[26], we opted for a more open orbital constraint by selecting lower-end values $k_3/k_2 = 0.39$ and $k_4/k_2 = 0.26$. Note that thermal histories compatible with orbital constraints would still exist for more restrictive (*i.e.*, larger) values of k_{3p}/k_2 and k_3/k_2 within the plausible range listed above.

In addition to the presence of the correction factor f and the simplifications mentioned above, the dissipation contributions of Phobos that appear in the equations 3 and 4 of *Heller, et al. [2011]*[22] have been replaced by expressions that are more appropriate in the case of tidal locking[28] we considered in our study. Therefore, the second terms on the right hand side of Eq. (24)

and Eq. (25) correspond to the expressions in equations A2 of *Lainey, et al. [2012]*[29]. Although these dissipation terms were found to be small, we kept them for completeness.

Table 3 summarizes the meaning and the values of the main parameters involved in the orbital evolution modeling.

S3 Computation of Mars' tidal quality factor, and Love number

The mass of Phobos being small, its influence on Mars is negligible. This results in a one-way coupling between the thermal evolution of Mars and the orbital evolution of Phobos. Such coupling mainly occurs through Mars' tidal quality factor Q, and to a smaller extent through its Love number k_2. The latter is less sensitive to temperature because it depends on Mars' mantle shear modulus, μ, that exhibits a relatively weak sensitivity to temperature[30,31], as long as large-scale melting does not take place within the last 4 Gyr of evolution. As mentioned earlier, such outcome would immediately lead to extremely small Q values[32], and the corresponding thermal evolution would be incompatible with orbital constraints. Since we have purposely excluded these solutions (section S5), one can rule out this possibility.

Both Q and k_2 appear in the orbital evolution equations (Eq. (24) and Eq. (25)) through the term Z'_p (Eq. (27)).

To compute Q and k_2 we followed the approach described elsewhere[33]. The displacement vector, $\mathbf{u}$, within a layered, elastic, self-gravitating, and spherically symmetric Mars is first computed by solving the following equation of motion[34] expressed below in terms of seismic velocities for P and S waves v_p, v_s (rather than Lamé coefficients):

$$\frac{\partial^2 \mathbf{u}}{\partial t^2} = (v_p^2 - v_s^2)\nabla(\nabla \cdot \mathbf{u}) + v_s^2 \nabla^2 \mathbf{u} + \nabla\psi + \mathbf{g}, \tag{28}$$

where $\mathbf{g}$ is the gravity vector, and ψ is the gravitational potential, which is is governed by the following Poisson equation:

$$\nabla^2 \psi = 4\pi G \nabla(\rho \mathbf{u}) \ . \tag{29}$$

Eq. (28) and Eq. (29) thus require the knowledge of density, ρ, and body-wave speeds. In addition, bulk and shear quality factors are needed to account for frequency effects on seismic velocities[35–37], and to compute the non-elastic contributions of k_2, as explained later. Given the spherical symmetry, these quantities are functions of the radial coordinate r. To determine them, the spherical domain is discretized into n_r radial grid points (we typically used 150-200) along which the entire temperature profile $T(r)$ is reconstructed with the knowledge of T_m, T_c, T_l, D_l, D_{cr}, δ_u, δ_c, the temperature within the lid obtained from the integration of Eq. (21) , and accounting for the adiabatic gradients within the mantle and the core. Along the same points we considered a given reference temperature profile $\bar{T}(r)$, which is associated with the following information: density ($\bar{\rho}$), body-wave velocities ($\bar{v}_p$, $\bar{v}_s$), bulk and shear quality factors ($\bar{Q}_\kappa$, $\bar{Q}_\mu$), and the temperature derivatives for body-wave velocities ($d\bar{v}_p/dT$, $d\bar{v}_s/dT$), and density ($d\bar{\rho}/dT$). Such a reference profile can be built[30,38] or borrowed from the literature[31]. Since the crustal thickness in our models evolves with time, computing at each time step the reference profile was more appropriate.

The reference pressure profile is calculated by integrating the hydrostatic equation $dP = -\rho g dr$ together with a Poisson equation $dg/dr = 4\pi r^2 G\rho - 2g/r$ in the mantle and in the core[26,38,39]. The reference temperature profile is chosen

as a hyperbolic tangent function in the silicate envelope[26], and a constant potential temperature in the core, to which the contributions of adiabatic gradients were added:

$$\bar{T} = \begin{cases} T_s + (T_m - T_s) \tanh\left(\frac{R_p - r}{D_l}\right) \left(1 + \alpha_m \; g \frac{R_p - r}{C_m}\right), & \text{if } r > R_c \\ T_c \left(1 + \alpha_c \; g \frac{R_p - r}{C_c}\right), & \text{if } r \leq R_c. \end{cases} \tag{30}$$

The mantle reference density and seismic velocity profiles were taken from *Nimmo and Faul [2013]*[26], which account for olivine-to-wadsleite and wadsleite-to-ringwoodite phase changes. For the liquid core (assumed to be composed of iron plus sulfur), we used $\bar{\rho}(r \leq R_c) = \rho_{c0}(1 + P/K)$, $\bar{v_p}(r \leq R_c) = \sqrt{K/\bar{\rho}}$) (where $\rho_{0c} = \rho(P = P_{CMB}) = 5400$ kg/m^3 and the bulk modulus K is assumed to vary with pressure as: $K = 110 + 2 \; P$ GPa[40]), $v_s(r \leq R_c) = 0$.

In the crust, we set $\bar{\rho} = 2900$ kg/m^3, $\bar{v}_p = 6690$ km/s, and $\bar{v}_s = 3860$ km/s[31].

The temperature derivatives of density and body-wave velocities in the silicate envelope where expressed as a second-order polynomial[31]:

$$\frac{dX}{dT} = X \; (B_0 + B_1 P + B_2 P^2) \; 10^{-4}, \tag{31}$$

where X represents $\bar{\rho}$, $\bar{v}_p$, or $\bar{v}_s$, and the coefficients $\{B_0, B_1, B_2\}$ are $\{-0.3647, 0.0121, -0.0002\}$ for density, $\{-0.9112, 0.0411, -0.0007\}$ for v_p, and $\{-0.9145, 0.0137, 0.0004\}$ for v_s. In the core, $d\bar{\rho}/dT$ was set to α_c, while we neglected the temperature sensitivity of P-waves velocity.

With the knowledge of the temperature difference between a given model and the reference profile, $\Delta T(r) = T(r) - \bar{T}(r)$, one can infer the density and seismic velocity profiles:

$$\rho(r) = \bar{\rho}(r) + \Delta T(r)\frac{d\bar{\rho}}{dT}(r), \tag{32a}$$

$$v_p(r) = \bar{v}_p(r) + \Delta T(r)\frac{d\bar{v}_p}{dT}(r), \tag{32b}$$

$$v_s(r) = \bar{v}_s(r) + \Delta T(r)\frac{d\bar{v}_s}{dT}(r)\ . \tag{32c}$$

The above linearization was proven to be sufficiently accurate, provided that $|\Delta T(r)|$ remains modest (*i.e.*, less than ∼500 K)[31]. Note that in the above relationships the frequency-dependent parameters are taken at tidal frequencies[35–37].

Making the reasonable assumption that bulk attenuation is negligible, $Q_\kappa(r) = \bar{Q}_\kappa(r) = 5.78\ 10^5$ by analogy with the Earth[41]. On the other hand, shear attenuation in the mantle is thought to vary according to[42]:

$$Q = Q_0 \left[\omega \exp\left(\frac{E^* + PV^*}{RT}\right)\right]^{\alpha_q} \tag{33}$$

where E^*, V^*, P, T, R have the same meaning than those described earlier, the power-law slope α_q is a constant taken equal to 0.1 (*i.e.*, a weak frequency dependence of Q[43]), ω is the frequency, and Q_0 is a constant adjusted to match Mars' value of $Q/k_2 = 559$ at present-day[44], whose computing procedure is detailed in the next section. In the liquid core, $\bar{Q}_\mu = 0$. In the frame of an absorption band model[45] we therefore assume that Mars' attenuation remains in the same frequency band. Deep mantle melt production reduces the value of the quality factor according to[32]:

$$Q(r, \bar{\phi}(r) > 0) = \frac{Q(r, \bar{\phi}(r) = 0)}{a_Q \ln[100\bar{\phi}(r)] + b_Q}, \tag{34}$$

where the constants $a_q = 2.406\ 10^{-2}$ and $b_q = 5.9284\ 10^{-2}$ for shear attenuation, and $a_q = 1.10173\ 10^{-2}$ and $b_q = 2.6518\ 10^{-2}$ for Q_κ. These empirical

expressions correspond to the experimental range $\bar{\phi} \cong$0.12-4%. Therefore, below this range Q is unaffected by melting. In addition, Q in the mantle is bounded to a minimum value of 10.

In addition, deep mantle melting affects seismic velocities:

$$v_p(r, \bar{\phi}(r) > 0) = \max[v_p(r)(1 - 20\bar{\phi}(r)), v_p^{\text{liq}}], \tag{35a}$$

$$v_s(r, \bar{\phi}(r) > 0) = \max[v_s(r)(1 - 10\bar{\phi}(r)), v_s^{\text{liq}}], \tag{35b}$$

which reproduce well the experimental trends observed in [32]. For large melt fractions, seismic velocities in the above expressions are bounded by the values of body waves speeds in CaO-MgO-Al_2O_3-SiO_2 liquids, set to $v_p^{\text{liq}} = \sqrt{(24\ 10^9 + 6P)/\rho(r)}$ [46]. For v_s^{liq}, we used 500 km/s instead of ~ 0 km/s for numerical convenience. This relatively high threshold value should however not significantly affect our results, because the main effect of mantle melting remains a strong and abrupt decrease in the quality factor. We made the reasonable assumption that the influence of deep mantle melting on densities is small compared to that on seismic velocities. Consequently, we neglected changes in density due to melting in the deep mantle.

With the knowledge of body-wave velocities, attenuation and density profiles, one can solve the equation of motion in a self-gravitating sphere (Eq. (28) Eq. (29)), which can be reduced to a set of ordinary differential equations [34,47]. This yields the real part of the Love number.

To account for viscous effects (corresponding to the complex part of k_2) Fréchet derivative of the real part is performed [33]. Then, with the knowledge of both real and imaginary parts of k_2, Q may be computed from:

$$Q = \frac{|k_2|}{Im(k_2)}. \tag{36}$$

An example of the radial profiles is displayed in Fig. S4, which agrees reasonably well with published radial models of Mars[30,31,38].

The calculation of Q_0 is performed once per thermo-chemical history, however, the procedure detailed above to compute Q is performed at each time step during the integration of the orbital evolution equations.

S4 Thermal-orbital coupling procedure

The thermo-chemical evolution equations (Eq. (2) and Eq. (3)) are integrated forward in time, starting from $t = 0$ until $t = 4.5$ Gyr. However, since Q_0 in Eq. (36) can only be determined with the knowledge of the present-day thermo-chemical state, and since the values of the orbital parameters at initial time are unknown, the orbital evolution equations (Eq. (24) and Eq. (25)) must be integrated backwards in time. We therefore proceed as follows:

1. Eq. (2) and Eq. (3) are integrated forward in time from $t = 0$ until present.

2. Using the obtained present-day thermo-chemical state, Q_0 is adjusted to yield $Q/k_2 = 559$[44]. To match this requirement, we used a bisection method, which typically converges within 2-5 iterations. The corresponding values of k_2 were found to be in good agreement with the latest estimates[48].

3. With the knowledge of Q_0 and the previously computed thermal history, Eq. (24) and Eq. (25) are integrated backward in time with $a = a_{\rm present} = 2.76\ R_p$ and $e = e_{\rm present} = 0.0151$ as starting conditions. Mars' tidal quality factor is constantly updated during the time-integration, according to the recorded thermal history. The integration proceeds until Phobos' semi-major axis reaches 99.99% of of synchronous radius $a_{\rm sync} = (GM_p/\omega_p^2)^{1/3}$, or until reaching the initial time $t = 0$.

The thermo-chemical and orbital evolution equations were integrated using a second-order Runge-Kutta (RK) method, with a step size ΔT chosen to be less than 1% of the shortest dynamical time *i.e.*, $\Delta t < 10^{-2} \min(X/(dX/dt))$, where X refers here to the time-dependent variables: T_m, T_c, D_l, D_{cr}, a, e. Our tests have shown that with such a requirement, the integration scheme was sufficiently accurate, and no significant differences were found with results obtained using fourth-order RK integration.

Eq. (24) and Eq. (25) lead to an increase in Phobos' semi-major axis and eccentricity when going backward in time. In the time interval t=[0-500] Myr where e is maximum, we found that the eccentricity ranges between 0.1 and 0.13. While the expressions we used to model Phobos' orbital evolution are accurate to second-order in e, the largest eccentricity values obtained are below the threshold $e \cong 0.3$ above which inaccuracies become unacceptably large[22,49]. While accounting for orbital evolution with higher accuracy in e is possible, such approach would introduce additional assumptions, which are not well understood yet[50]. For these reasons, we believe our formalism is well adapted to our modeling problem.

Table 2 lists the values of several key parameters involved in the computation of the quality factor.

S5 Systematic exploration procedure and confrontation of the results with constraints

We conducted a systematic exploration of the following parameter space: $E^* = [60 - 350]$ kJ/mol, $V^* = [0 - 6]$ cm^3/mol, $T_{m0} = [1700 - 2000]$ K, $T_{c0} = T_{m0} + [100 - 500]$ K. The parameter space mentioned above represents a total of $\sim 10^5$ evolutions that were confronted to thermal and orbital constraints (see below). This exploration was performed in parallel, using the MPI library.

The relatively low values of activation energy (< 200 kJ/mol) considered would correspond to mantle deformation with a dislocation creep mechanism[1–4].

The vast parameter space explored can be reduced by requiring that thermo-chemical and orbital evolutions satisfy the following three constraints detailed below. The first constraint concerns Mars' mantle secular cooling during the Amazonian-Hesperian time period (*i.e.*, from $\sim$3.6 Gyr ago, until present). Petrological considerations[51] suggest a relatively modest cooling rate of 30-40 K/Gyr for the Martian mantle during this time period, corresponding to a total cooling of $\sim$100-140 K. This constraint is illustrated in Fig. 1e and Fig. 2a.

The second constraint relates to the generation of a magnetic field during the first Gyr of Mars' evolution, as suggested by Mars' crustal magnetization[52]. Assuming that such a magnetic field was produced by an early thermal dynamo within Mars' fully molten core, we formulate this constraint using three requirements[53] listed below:

1. The heat flow out of the core, q_c, must exceed the adiabatic value: $q_a = k_c \alpha_c g_c T_c / C_c$, for convection within the core to occur.

2. The rate at which gravitational potential energy is released by convection must exceed a critical value given by the ratio of ohmic dissipation (normalized in what follows by the core surface area), $\Phi = \nu_{\rm mag} B^2/(3\mu_{\rm mag} R_c)$ (where B=2.5 mT is the magnetic field strength, $\nu_{\rm mag}$=2 m^{2}s^{-1} is the magnetic diffusivity, and $\mu_{\rm mag}=4\pi\ 10^{-7}$ H m^{-1} is the magnetic permeability), over $\epsilon_T = 0.8\pi\alpha_c G \rho_c R_c^2 (1 - q_a/q_c)/(3C_c)$, the Carnot efficiency style for thermal convection: $q_c > \Phi/\epsilon_T$.

3. The complexity of the convective motions measured by the magnetic Reynolds number, $Re_m = u_c R_c/\nu_{\rm mag}$ (where the characteristic velocity scale $u_c = [q_c \alpha_c g_c R_c/(\rho_c C_c)]^{1/3}$ for Mars' core is given by the force balance between inertia and buoyancy), must be sufficient to favor self-sustaining dynamo

action: $Re_m > 100$.

Using the three requirements above we can determine $t_{\mathrm{dyn_c}}$, the time at which the dynamo ceases to operate (Fig. 1f), and the solutions that are compatible with the presence of an early magnetic field: $0 < t_{\mathrm{dyn_c}} < 1$ Gyr (Fig. 2b).

The last constraint concerns the orbital evolution of Phobos, whose semi-major axis is required to be less than the synchronous radius $a_{\mathrm{sync}} = 6.03$ for the last four billion years of Mars' evolution. This requirement comes from the fact that Phobos is currently located well within the synchronous radius, and that it must have been emplaced also within this limit during the first 500 Myr of Mars' evolution. Otherwise, like Deimos, Phobos would be currently moving away from Mars, or would remain at or very close to the synchronous limit. Along each orbital evolution calculation (see section S2), we monitor backward in time t_{sync}, the time at which Phobos semi-major axis reaches 99.99% of the synchronous radius (Fig. 1g). The evolution is considered to be compatible with our orbital constraint only if $t_{\mathrm{sync}} < 0.5$ Gyr (Fig. 2c). Note that the compatibility of Phobos' orbital evolution is in fact governed by Mars' thermo-chemical evolution (mainly through the value of Mars' tidal quality factor Q, as discussed earlier), which depends on its initial thermal state and its rheology. Fig. S3 illustrate such influences: it depicts the thermal-orbital evolution of two cases which differ only from the value of the reference viscosity. We considered a 'low' viscosity case $\eta_0 = 1.7\ 10^{20}$ Pa s, and a 'high' viscosity case, $\eta_0 = 1.7\ 10^{22}$ Pa s. The different rheologies between the two cases result in distinct thermal evolutions (Fig. S3a), where the lower viscosity case results in a more vigorous mantle convection, thus a more efficient cooling. The resulting cooling histories imply distinct evolution of Mars' tidal quality factor (Fig. S3b), where the colder case evolves, backward in time, toward lower values of the tidal quality factor. This, in turn, leads to a more rapid increase of Phobos' semi-major axis (also going

backward in time), hence a value of $t_{\rm sync} = 0.71$, which is incompatible with the assumption according to which Phobos was emplaced within the synchronous radius during the first 500 Myr of Mars' evolution. On the contrary, the more viscous, slowly cooling case exhibits a smaller value of $t_{\rm sync} = 0.46$, which is compatible with orbital evolution constraints.

Finally, the simultaneous satisfaction of the three constraints mentioned above drastically reduces the solution space (*e.g.*, Fig. 2d). Often (but not systematically) secular cooling and magnetic constraints define similar areas (Fig. 2d), which would not allow one to put tighter constraints on Mars' mantle rheology, due to its trade-off with temperature, or due to the trade-offs between different rheological parameters (*e.g.*, η_0, E^*). The additional use of the orbital evolution constraints largely eliminate these trade-offs. In some cases (*e.g.*, Fig. S5), secular cooling and magnetic constraints do not superimpose, leading to a set of mantle rheological parameters that is not compatible with all constraints.

S6 Effect of additional early processes on model results

In this section we consider the influence of two potential complexities on the thermal and orbital evolution results.

S6.1 Influence of early plate tectonics

With the exception of the Earth, stagnant lid convection is a common state at which terrestrial planets evolve. While Mars falls into such category, it has been argued that plate tectonics could have operated during the first few hundreds of millions of years of its evolution ([54] and references therein). Although this scenario remains debated, we have investigated the potential effect of early plate tectonics occurring during the first 500 Myr of Mars' evolution, following the

approach described in[54]. The presence of early plate tectonics has a significant impact on Mars' thermal evolution, thus also on Phobos' orbital evolution. Early plate tectonics allows a more efficient convective heat transfer, which yields colder mantle and core evolutions (Fig. S6a). This implies a weaker tidal dissipation in the mantle when early plate tectonics operates (Fig. S6b). Although this has a tendency to yield smaller values of semi-major axis and $t_{\rm sync}$ values, the overall effect is moderate (Fig. S6c-d). This can also be appreciated by comparing Fig. 2c and Fig. S7c, which display the area satisfying the orbital constraints ($t_{\rm sync} < 0.5$ Gyr) for two cases differing only from the presence or the absence of early plate tectonics. However, early plate tectonics has a much stronger influence on secular cooling and magnetic constraints. Indeed, by allowing for a more rapid core and mantle cooling, early plate tectonics strongly shifts the area of the matching secular cooling constraints toward lower activation energies, particularly at low reference viscosities (compare Fig. 2a and Fig. S7a). Therefore, these changes affect primarily a solution space that does not match all the constraints we considered (Fig. S7d). In addition, the more efficient heat extraction during the first 0.5 Gyr favors the presence of an early dynamo, and therefore significantly broadens the area of solutions that satisfy the magnetic constraints (compare Fig. 2a and Fig. S7b). Overall, the main influence of early plate tectonics is the shift of secular cooling constraints toward lower values of activation energy (Fig. S7d). This is also illustrated in Fig. S8 that shows statistics of present-day and time-averaged quantities of the matching solutions for the entire parameter space considered when accounting for early plate tectonics.

While the presence of early plate tectonics weakly affects the fraction of the matching solution, it does lead to a reduction in the activation volumes: $V^*_{\rm disl} <$ 10.5 cm^3/mol instead of $V^*_{\rm disl} < 14$ cm^3/mol (compare Fig. S8a and Fig. 3a). In

addition, early plate tectonics shifts matching solutions toward lower values of activation energy: 250 ± 40 kJ/mol (Fig. S8c) instead of 280 ± 80 kJ/mol when early plate tectonic is absent (Fig. 3c). The predicted range of present-day crustal thickness is also lowered to $D_{\rm cr} \cong 30 \pm 20$ km (compare Fig. S8e and Fig. S3e). All other quantities (reference mantle viscosity and surface heat flux), are weakly affected by the presence of early plate tectonics (compare Fig. S8b,d and Fig. 3b,d).

In summary, even though early plate tectonics significantly affects Mars' thermal evolution, it primarily influences solutions that do not satisfy simultaneously orbital, secular cooling, and magnetic constraints. Overall, it results in only moderate differences with respect to the case where early plate tectonics is absent.

S6.2 Influence of an early surface ocean of liquid water

The early surface of Mars was likely covered by an ocean of liquid water[55,56]. On Earth, the presence of liquid water at the surface currently accounts for the majority ($\sim 80\%$) of tidal dissipation, due to friction along shorelines and at the bottom of the ocean, in regions where the bathymetry is rough[57–59]. It is therefore legitimate to investigate the influence of such an early Martian ocean on the orbital evolution of Phobos. While the presence of a surface ocean would likely decrease the value of Mars' tidal quality factor, a precise estimation of such decrease is not a trivial task, due to a number of poorly constrained parameters, notably the extent and the longevity of the Martian surface ocean. To estimate the influence of the surface ocean on Mars' tidal quality factor we considered an ocean covering about a third of the surface during the first 800 Myr of Mars' evolution. Taking the Earth-Moon system as reference where $\sim 80\%$ of the tidal energy is currently dissipated into the oceans[57,59], the tidal quality factor reduction due to presence of oceans is $f_{\rm Q_{ocean}} = 80\%$. Assuming that dissipa-

tion is proportional to the surface fraction covered by the ocean, this decreases $f_{\mathrm{Q_{ocean}}}$ to 40%, because the area extent of the Martian ancient ocean was likely twice smaller than that of present-day Earth. In addition, we assumed that the ocean was persistent 50% of time window during which surface liquid water was possible via cyclic episodes[56,60], thereby further reducing $f_{\mathrm{Q_{ocean}}}$ to 20%. Consequently, we accounted for the presence of an early surface ocean reducing Mars' tidal quality factor by 20% during the first 800 Myr of its evolution. The corresponding results are summarized in Fig. S9. As expected, the increase in tidal dissipation due to the early ocean reduces the matching solution space (compare Fig. S9a and Fig. 3a). The corresponding ranges of solutions is also narrower with reference viscosities $\eta_0 \cong 10^{22.7\pm0.1}$ Pa s (compare Fig. S9b and Fig. 3b), and dislocation creep activation energies $E^*_{\mathrm{disl}} \cong 220 \pm 25$ kJ/mol (Fig. S9c). The range of present-day heat flux values: 20 ± 0.5 mW/m^2 (Fig. S9d), is narrower but comparable to that obtained without the presence of an ocean (Fig. 3d), and the range of predicted values for the present-day crustal thickness is even narrower: $D_{cr} = 33 \pm 2$ km (compare Fig. S9e and Fig. 3e).

One should note, however, that the chosen value of $f_{\mathrm{Q_{ocean}}}$=20% is likely an upper bound, because the Martian paleo-bathymetry is smooth compared to that of the Earth. Therefore, dissipation at the bottom of the ocean floor, estimated on Earth to account for about 30% of the total tidal energy[58], may have been negligible on Mars, implying that the effect of an early Martian ocean may have been even smaller.

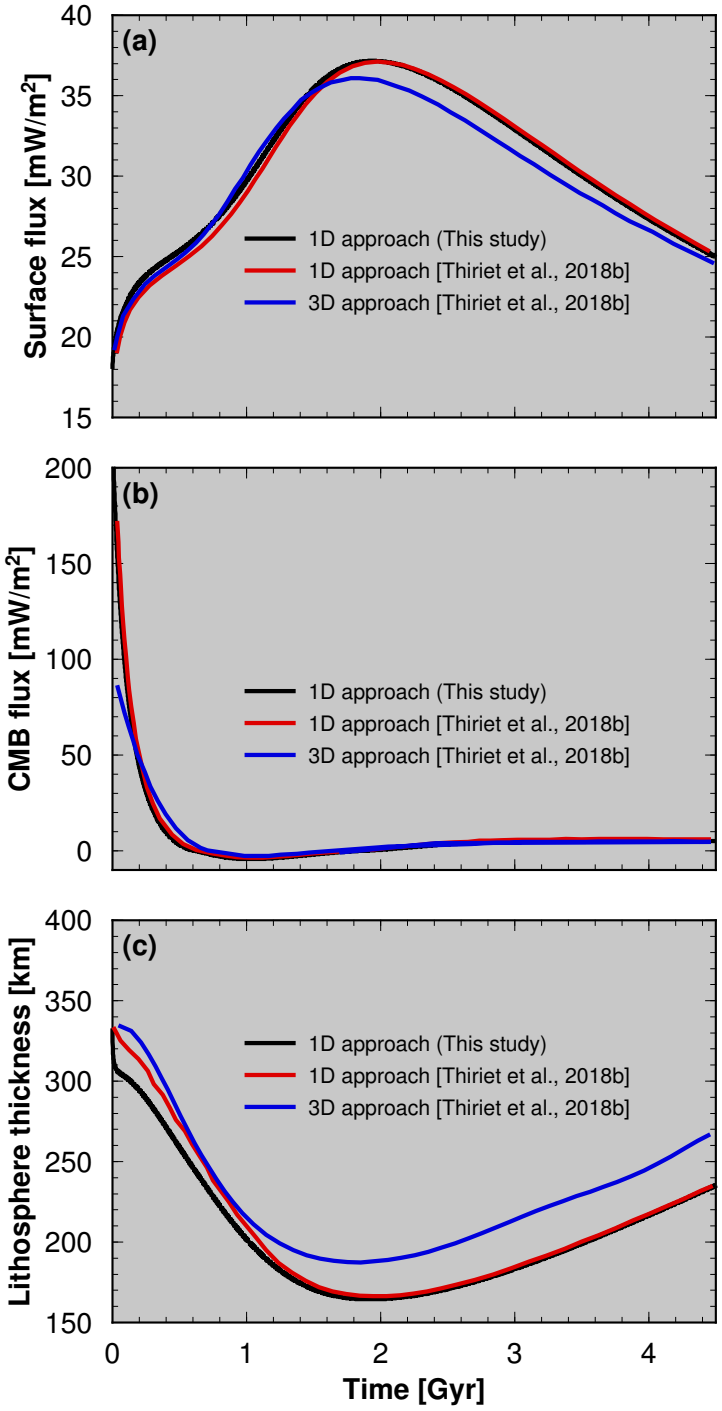

Figure S 1: Comparison between parameterized models and fully 3D spherical models of Mars' thermal evolution | Time evolution of Surface heat flux (a), CMB heat flux (b), and lithospheric thickness (c). The results of our parameterized convection model (black curves) is compared with the parameterized models of *Thiriet et al., 2018*[9] (red curves) and the 3D calculations also shown in *Thiriet et al.*[9] (blue curves).

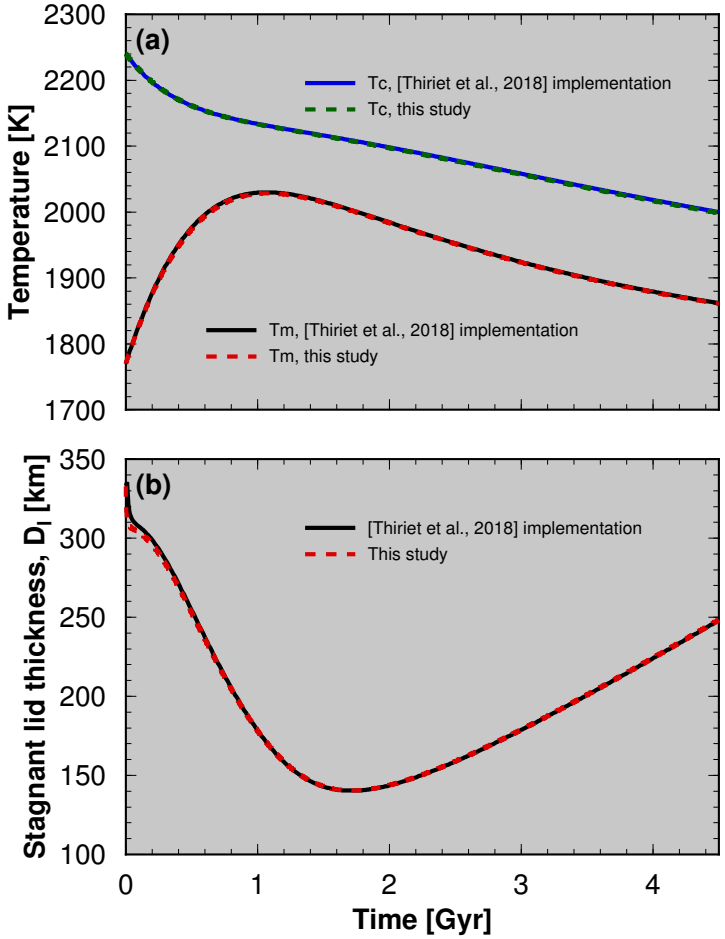

Figure S 2: Benchmark for the numerical implementation of the parameterized convection models.| Comparison of our implementation (dashed curves) of the governing equations for Mars' thermal evolution model (section S1) with that used in *Thiriet et al.*[3,9] (plain curves). (a) CMB and Mantle temperature beneath the lithospheric lid. (b) Stagnant lid thickness.

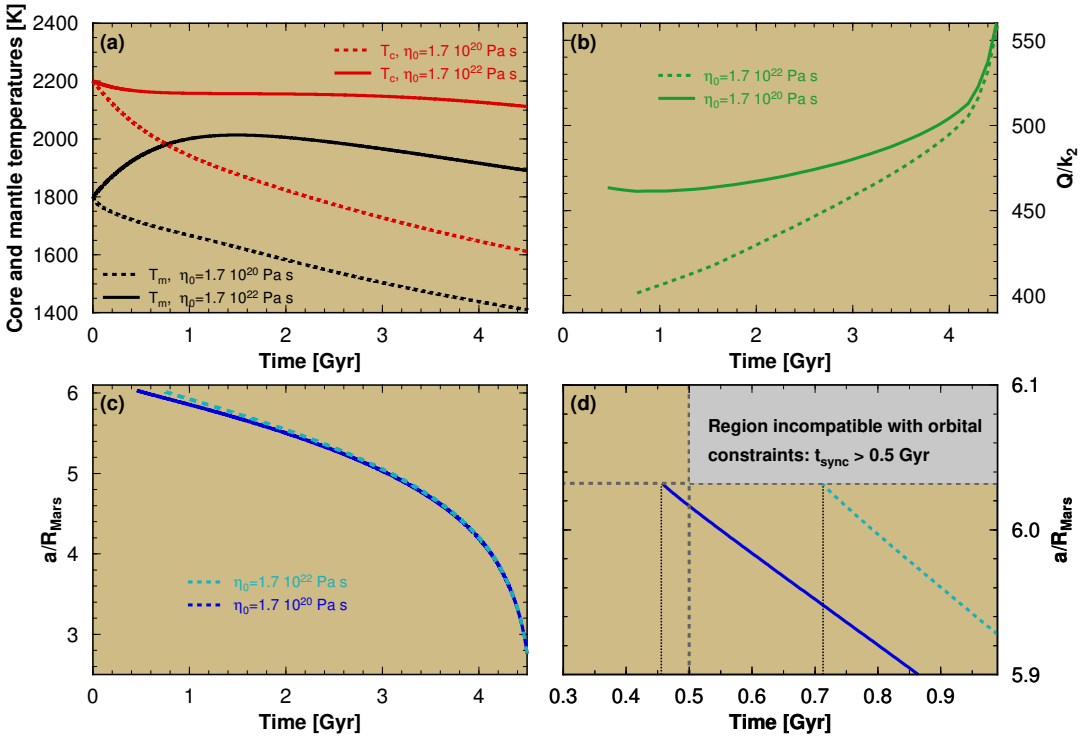

Figure S 3: Effect of rheology on the orbital evolution of Phobos| (a) Thermal evolution of the mantle (black curves) and the core (red curves) for two cases which differ only from the value of the reference viscosity. We considered a 'lower' viscosity case $\eta_0 = 1.7\ 10^{20}$ Pa s (dotted lines), and a 'high' viscosity case: $\eta_0 = 1.7\ 10^{22}$ Pa s (plain lines). Other rheological parameters are: $E^* = 90$ kJ/mol, $V^* = 0$ cm^3/mol. Time evolution of Mars' tidal quality factor (b), and Phobos' semi-major axis normalized by Mars' radius (c). (d) Zoom on a restricted portion of (c). The grey area shows the region where the time $t = t_{\rm sync}$ at which Phobos reaches 99.99% of the synchronous radius is larger than $t = 0.5$ Gyr, the higher limit of Phobos emplacement. In this example, $t_{\rm sync} = 0.71$ Gyr for the 'low' viscosity case, which is incompatible with the orbital constraint, and $t_{\rm sync} = 0.46$ Gyr for the 'high' viscosity case, which is compatible with the orbital constraint.

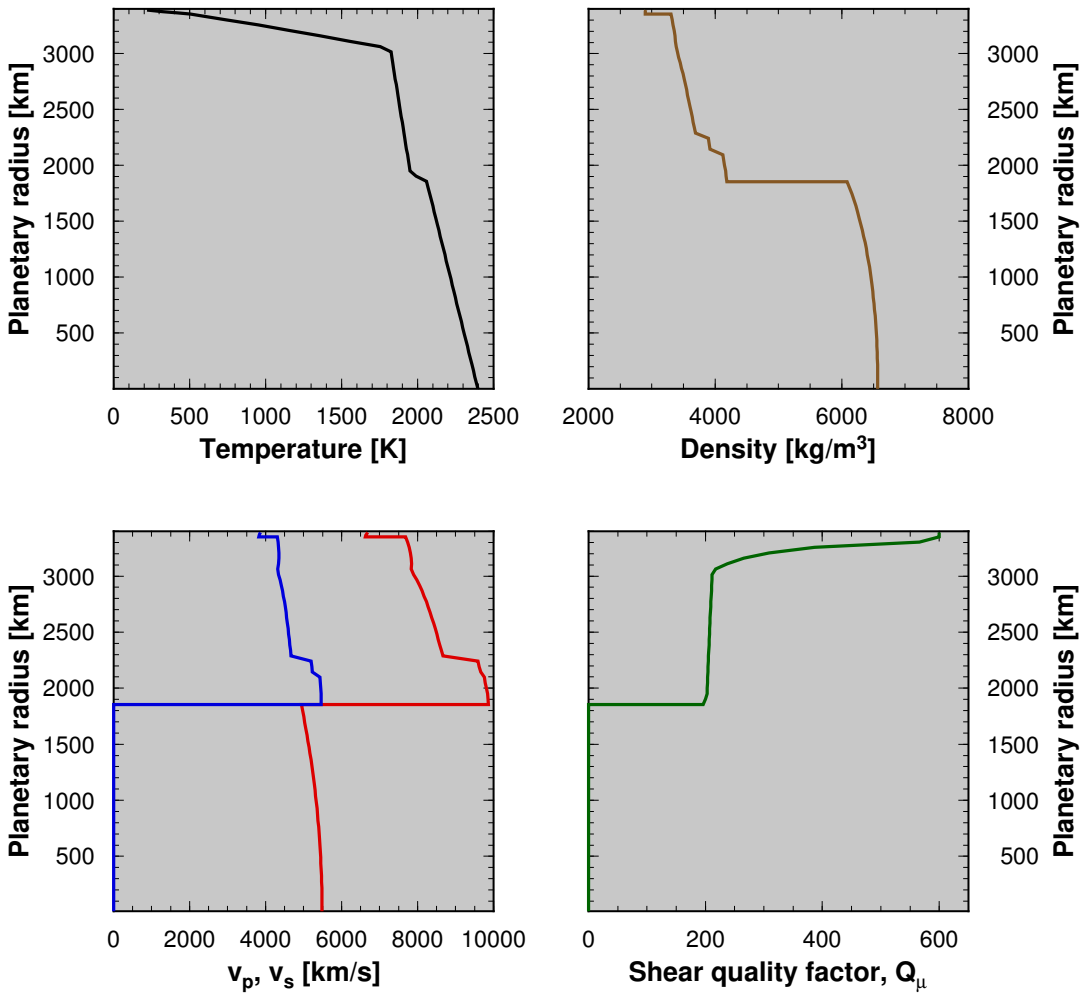

Figure S4: Example of Mars' radial profiles computed at present-day| (a) Thermal profile reconstructed from the knowledge of physical quantities from the parameterized convection model (*e.g.*, T_m, T_c, T_l, D_l, D_{cr}, δ_u, δ_c ...). (b) Corresponding density profile. (c) Body-wave seismic velocities: P-waves (red), and S-waves (blue). (d) Shear quality factor. See text for further details.

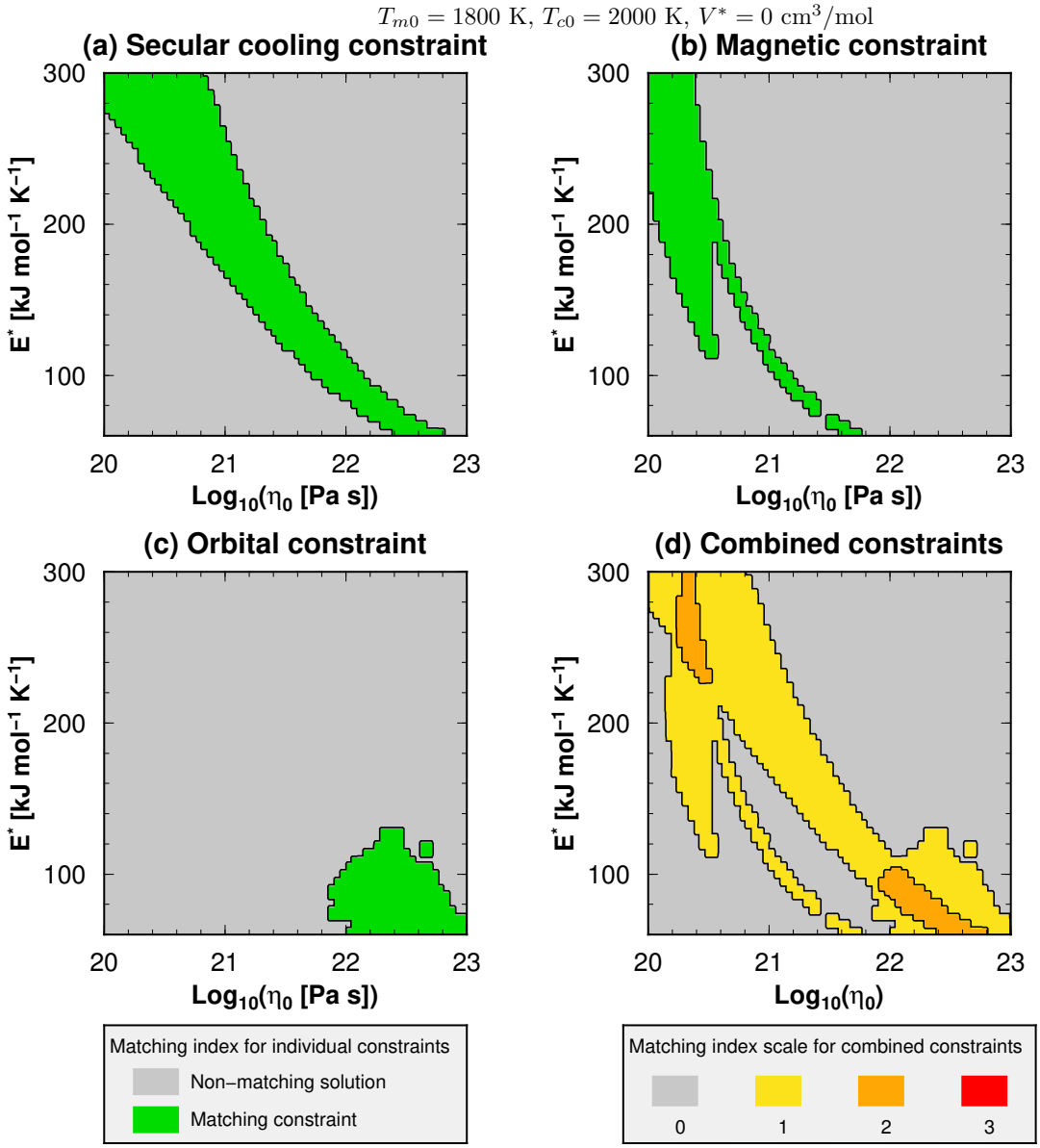

Figure S 5: Results from the exploration of Mars-Phobos' thermo-orbital evolution for an initial thermal state T_{m0} = 1800 K, T_{c0} = 2000 K and an effective activation volume V^* = 0 cm^3/mol. | Application of thermal and orbital constraints for a case that differs from Fig. 1 and Fig. 2 only from the value of the initial core temperature. (a-c) Individual constraints. (d) combined constraints. The warmer colors indicate a higher matching index, while grey areas indicate thermal evolution that are not compatible any constraints considered. Contrary to the case displayed in Fig. 2 red areas representing mantle rheologies that satisfy all constraints are absent. This indicates that this set of mantle rheological parameters cannot satisfy all constraints.

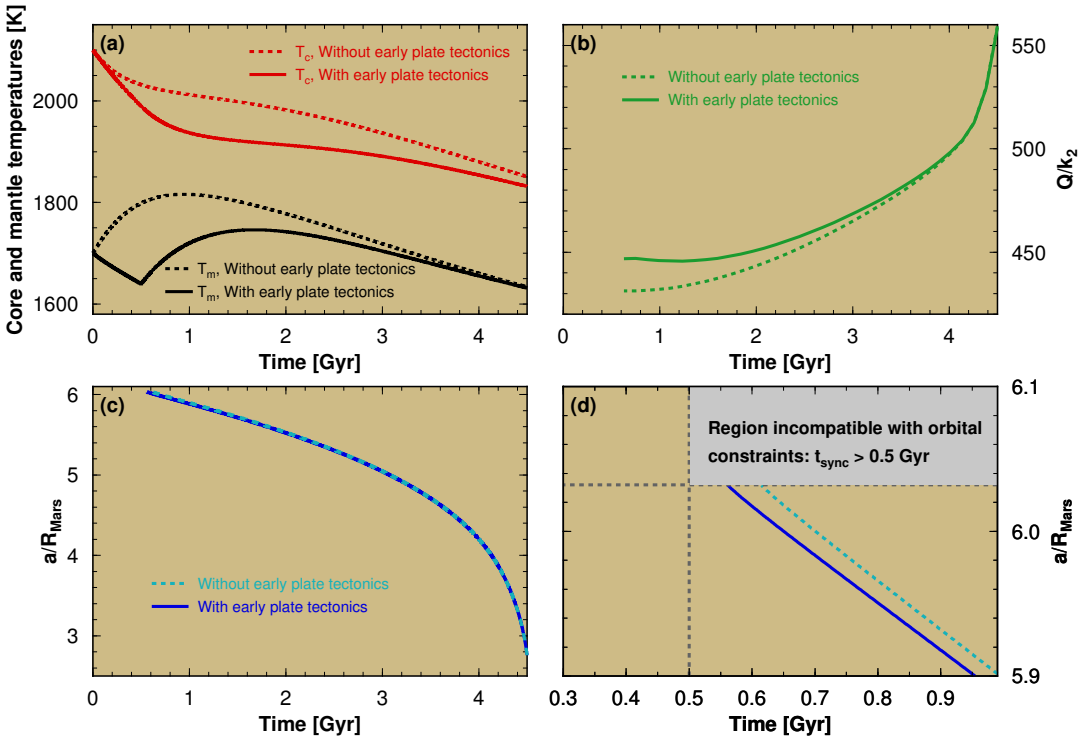

Figure S 6: Effect of early plate tectonics on the thermal-orbital evolution of Mars and Phobos| Evolution of two cases which differ only from the presence or the absence of plate tectonics operating during the first 500 Myr of Mars' evolution. The case with plate tectonics is displayed with plain curves, while the case without plate tectonics is shown by dashed curves. The thermal and rheological parameters are: $\eta_0 = 10^{21}$ Pa s, $E^* = 100$ kJ/mol, $V^* = 0$ cm^3/mol, T_{m0}=1800 K, T_{c0}=2200 K. (a) Thermal evolution of the mantle (black curves) and the core (red curves). Time evolution of Mars' tidal quality factor (b), and Phobos' semi-major axis normalized by Mars' radius (c). (d) Zoom on a restricted portion of (c). The grey area shows the region where the time $t = t_{\rm sync}$ at which Phobos reaches 99.99% of the synchronous radius is larger than $t = 0.5$ Gyr, the higher limit of Phobos emplacement.

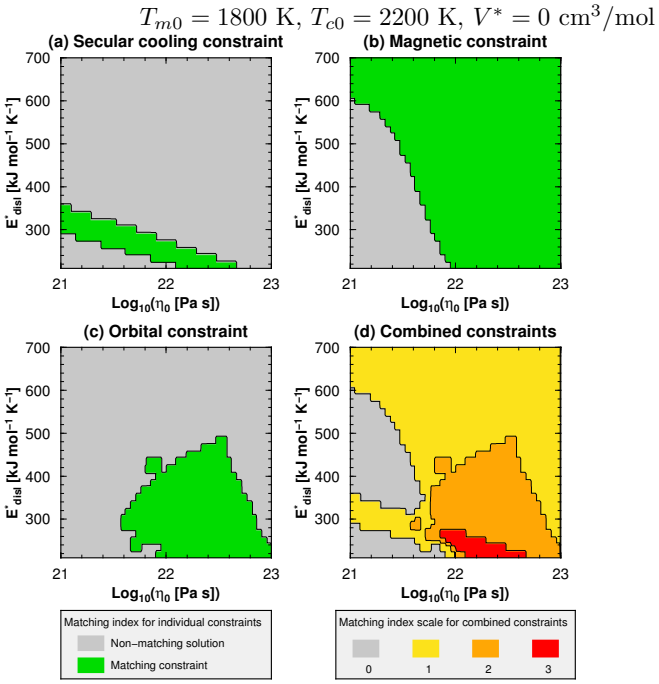

Figure S 7: Effect of early plate tectonics on Mars-Phobos' thermal-orbital evolution for an initial thermal state T_{m0} = 1800 K, T_{c0} = 2200 K and an effective activation volume V^* = 0 cm^3/mol. | Application of thermal and orbital constraints for a case that differs from Fig. 1 and Fig. 2 only from the value of the initial core temperature. (a-c) Individual constraints. (d) combined constraints. The warmer colors indicate a higher matching index, while grey areas indicate thermal evolution that are not compatible any constraints considered.

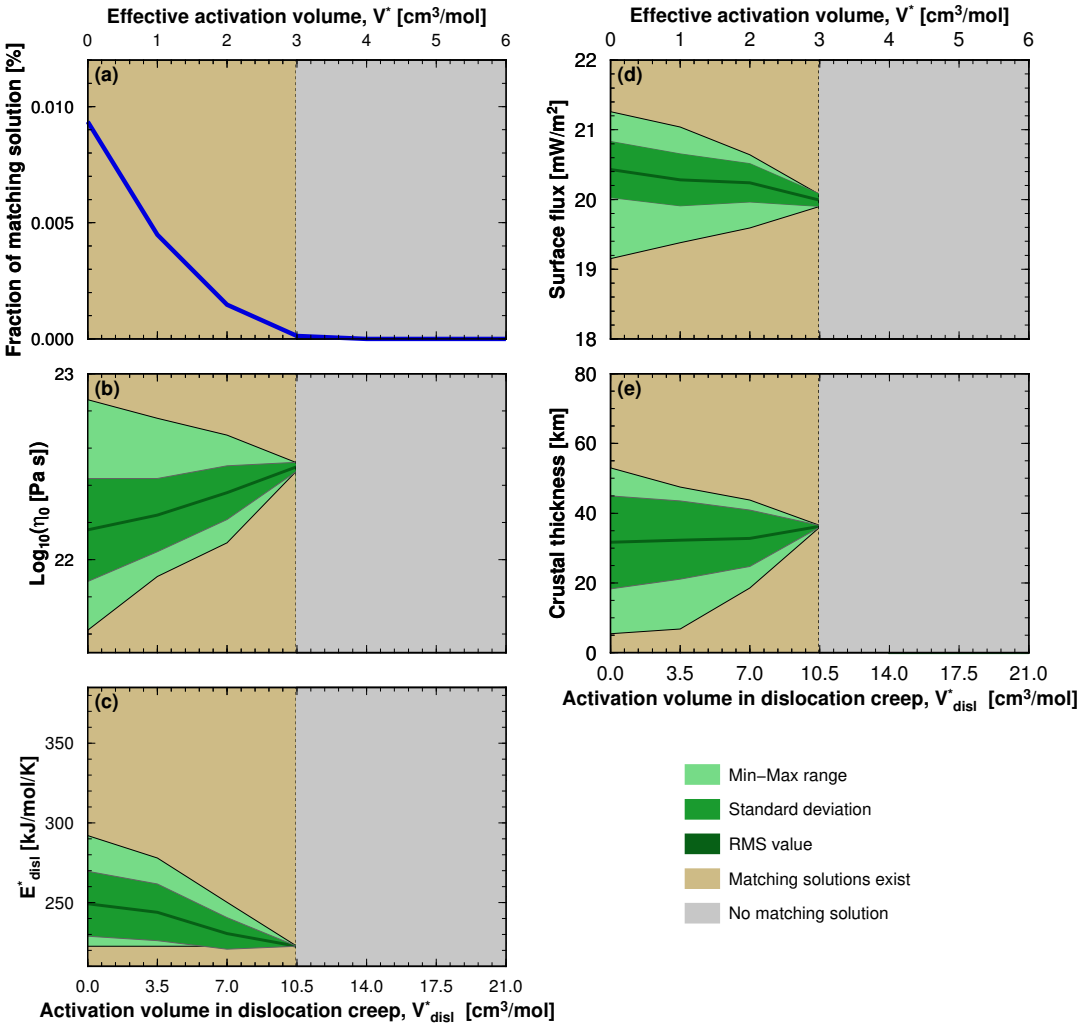

Figure S 8: Effect of early plate tectonics. Results from the exploration of Mars-Phobos' thermal-orbital evolution. | Statistics of present-day and time-averaged quantities of the matching solutions for the entire parameter space considered. The cases are identical to those displayed in Fig. 1(a-e) with the exception that they consider the presence of plate tectonics operating during the first 500 Myr of Mars' evolution.

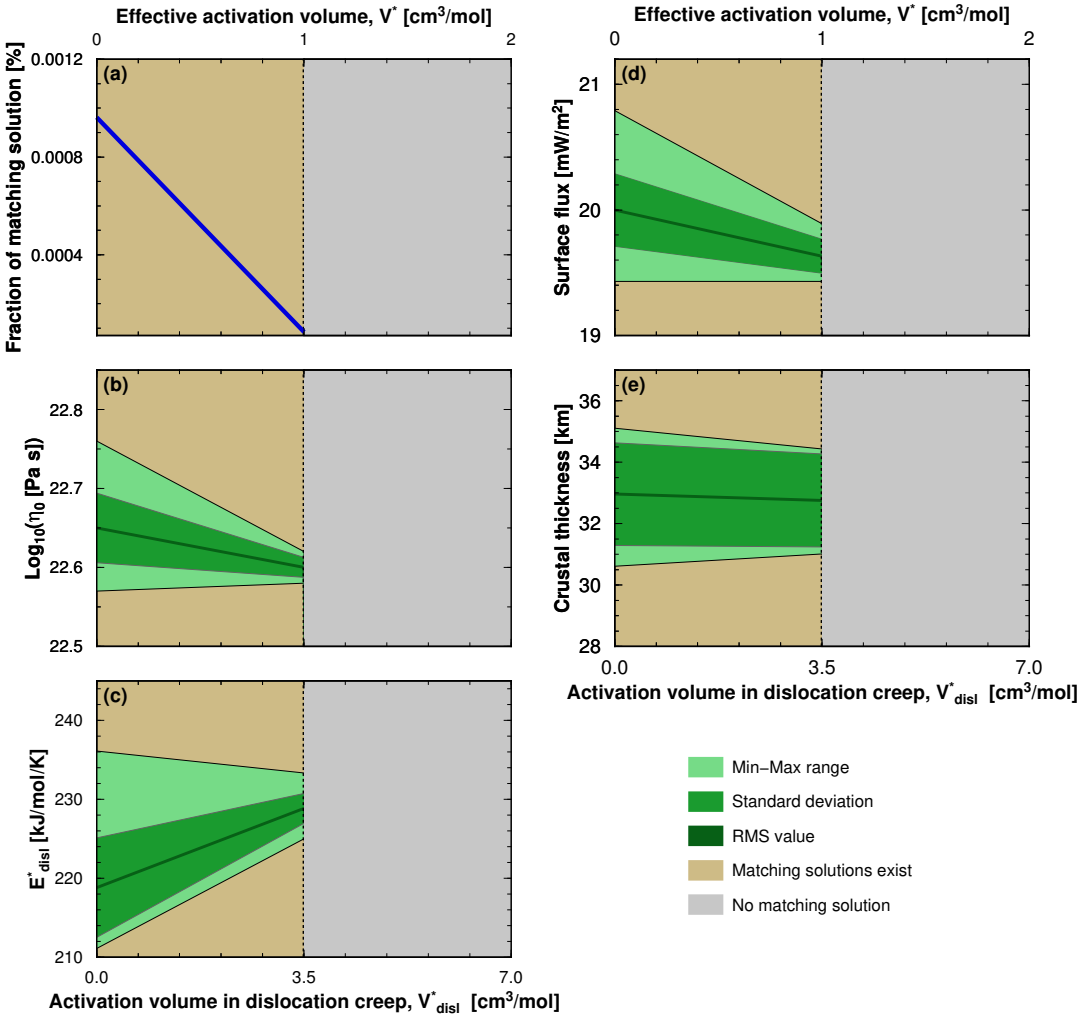

Figure S 9: Effect of an early surface water ocean. Results from the exploration of Mars-Phobos' thermal-orbital evolution. | Statistics of present-day and time-averaged quantities of the matching solutions for the entire parameter space considered. The cases are identical to those displayed in Fig. 1(a-e) with the exception that they consider the the presence of an ocean at the surface of Mars during the first 800 Myr of evolution.

References

[1] A.-C. Plesa, N. Tosi, M. Grott, and D. Breuer. Thermal evolution and Urey ratio of Mars. *Journal of Geophysical Research: Planets*, 120(5):995–1010, 2015.

[2] W. S. Kiefer and Q. Li. Water undersaturated mantle plume volcanism on present-day Mars. *Meteoritics & Planetary Science*, 51(11):1993–2010, 2016.

[3] M. Thiriet, C. Michaut, D. Breuer, and A.-C. Plesa. Hemispheric Dichotomy in Lithosphere Thickness on Mars Caused by Differences in Crustal Structure and Composition. *Journal of Geophysical Research: Planets*, 123(4):823–848, 2018.

[4] U. R. Christensen. Convection in a variable-viscosity fluid: Newtonian versus power-law rheology. *Earth Planet. Sci. Lett.*, 64:153–162, 1983.

[5] D. Breuer and T. Spohn. Viscosity of the Martian mantle and its initial temperature: Constraints from crust formation history and the evolution of the magnetic field. *Planet. Sp. Sci.*, 54:153–169, 2006.

[6] A. Morschhauser, M. Grott, and D. Breuer. Crustal recycling, mantle dehydration, and the thermal evolution of Mars. *Icarus*, 212(2):541–558, 2011.

[7] N. Tosi, M. Godolt, B. Stracke, T. Ruedas, J. L. Grenfell, D. Höning, A. Nikolaou, A. C. Plesa., D. Breuer, and T. Spohn. The habitability of a stagnant-lid Earth. *Astronomy and Astrophysics*, 605:doi:10.1051/0004–6361/201730728, 2017.

[8] A. Davaille and C. Jaupart. Transient High-Rayleigh-Number Thermal-Convection with Large Viscosity Variations. *J. Fluid Mech.*, 253:141–166, 1993.

[9] M. Thiriet, D. Breuer, C. Michaut, and A.-C. Plesa. Scaling laws of convection for cooling planets in a stagnant lid regime. *Phys. Earth. Pl. Int.*, 286:138–153, 2018.

[10] F. Deschamps and C. Sotin. Thermal convection in the outer shell of large icy satellites. *J. Geophys. Res.*, 106(E3):5107–5121, 2001.

[11] E. Takahashi. Speculations on the Archean Mantle - Missing Link Between Komatiite and Depleted Garnet Peridotite. *J. Geophys. Res.*, 95(B10):15941–15954, 1990.

[12] E. Ohtani, A. Suzuki, and T. Kato. Flotation of Olivine and Diamond in Mantle Melt at High Pressure: Implications for Fractionation in the Deep Mantle and Ultradeep Origin of Diamond, *American Geophysical Union monograph*, pages 227–239 ,1998.

[13] A.-M. Lejeune and P. Richet. Rheology of crystal-bearing silicate melts: An experimental study at high viscosities. *J. Geophys. Res.*, 100:4215–4229, 1995.

[14] C. Liebske, B. Schmickler, H. Terasaki, B. Poe, A. Suzuki, K. Funakoshi, R. Ando, and D. Rubie. Viscosity of peridotite liquid up to 13 GPa: Implications for magma ocean viscosities. *Earth Planet. Sci. Lett.*, 240(3-4):589–604, 2005.

[15] Y. Abe. Thermal and chemical evolution of the terrestrial magma ocean. *Phys. Earth. Pl. Int.*, 100:27–39, 1997.

[16] A. Salvador, H. Massol, A. Davaille, E. Marcq, P. Sarda, and E. Chassefière. The relative influence of H_2O and CO_2on the primitive surface conditions and evolution of rocky planets. *Journal of Geophysical Research: Planets*, 122(7):1458–1486, 2017.

[17] R. Merk, D. Breuer, and T. Spohn. Numerical Modeling of ^{26}Al-Induced Radioactive Melting of Asteroids Considering Accretion. *Icarus*, 159:183–191, 2002.

[18] A. H. Treiman, M. J. Drake, M.-J. Janssens, R. Wolf, and M. Ebihara. Core formation in the Earth and Shergottite Parent Body (SPB): Chemical evidence from basalts. *Geochim. Cosmochim. Acta*, 50(6):1071–1091, 1986.

[19] V. Stamenković, L. Noack, D. Breuer, and T. Spohn. The influence of pressure-dependent viscosity on the thermal evolution of super-earths. *Astrophysical J.*, 748(1):41–22, 2012.

[20] M. Thiriet. *Effect of the north/south dichotomy on the thermal structure and evolution of Mars*. PhD thesis, Université Sorbonne Paris Cité École Doctorale Step'Up, 2018.

[21] S. Ferraz-Mello, A. Rodriguez, and H. Hussmann. Tidal friction in close-in satellites and exoplanets: the Darwin theory re-visited. *Celestial Mechanics and Dynamical Astronomy*, 101(1-2):171–201, 2008.

[22] R. Heller, J. Leconte, and R. Barnes. Tidal obliquity evolution of potentially habitable planets. 528(A27):doi: 10.1051/0004–6361/201015809, 2011.

[23] P. Goldreich and R. Sari. Tidal evolution of rubble piles. *Astrophysical J.*, 691(1):54–60, 2009.

[24] S. Le Maistre, P. Rosenblatt, N. Rambaux, J. C. Castillo-Rogez, V. Dehant, and J.-C. Marty. Phobos interior from librations determination using

Doppler and star tracker measurements. *Planet. Sp. Sci.*, 85(c):106–122, 2013.

[25] B. G. Bills, G. A. Neumann, D. E. Smith, and M. T. Zuber. Improved estimate of tidal dissipation within Mars from MOLA observations of the shadow of Phobos. *J. Geophys. Res.*, 110(E7):doi:10.1029/2004JE002376, 2005.

[26] F. Nimmo and U. H. Faul. Dissipation at tidal and seismic frequencies in a melt-free, anhydrousMars. *J. Geophys. Res.*, 118(12):2558–2569, 2013.

[27] T. Van Hoolst, V. Dehant, F. Roosbeek, and P. Lognonné. Tidally induced surface displacements, external potential variations, and gravity variations on Mars. *Icarus*, 161(2):281–296, 2003.

[28] S. J. Peale and P. Cassen. Contribution of tidal dissipation to lunar thermal history. *Icarus*, 36:245–269, 1978.

[29] V. Lainey, Ö. Karatekin, J. Desmars, S. Charnoz, J.-E. Arlot, N. Emelyanov, C. Le Poncin-Lafitte, S. Mathis, F. Remus, G. Tobie, and J.-P. Zahn. Strong tidal dissipation in saturn and constraints on enceladus' thermal state from astrometry. *Astrophysical J.*, 752(1):14, 2012.

[30] A. Rivoldini, T. Van Hoolst, O. Verhoeven, A. Mocquet, and V. Dehant. Geodesy constraints on the interior structure and composition of Mars. *Icarus*, 213(2):451–472, 2011.

[31] S. E. Smrekar, P. Lognoné, T. Spohn, B. Banerdt, D. Breuer, U. Christensen, V. Dehant, M. Drilleau, W. Folkner, N. Fuji, R. Garcia, D. Giardini, M. Golombek, M. Grott, T. Gudkova, C. Johnson, A. Khan, B. Langlais, A. Mittelholz, A. Mocquet, R. Myhill, M. Panning, C. Perrin, T. Pike, A.-C. Plesa, A. Rivoldini, H. Samuel, T. van Hoolst, O. Verhoeven, R. Weber,

and M. Wieczorek. Pre-mission insights on the interior of mars. *Space Science Reviews*, 215:doi:10.1007/s11214–018–0563–9, 2019.

[32] J. Chantel, G. Manthilake, D. Andrault, D. Novella, T. Yu, and Y. Wang. Experimental evidence supports mantle partial melting in the asthenosphere. *Science advances*, 2(5):doi:10.1126/sciadv.1600246, 2016.

[33] A. Khan, K. Mosegaard, J. G. Williams, and P. Lognonné. Does the Moon possess a molten core? Probing the deep lunar interior using results from LLR and Lunar Prospector. *J. Geophys. Res.*, 109(E9):80, 2004.

[34] Z. Alterman, H. Jarosh, and C. L. Perekis. Oscillations of the Earth. *Proceedings of the Royal Society A: Mathematical, Physical and Engineering Sciences*, 252(1268):80–95, 1959.

[35] H. Kanamori and D. L. Anderson. Importance of Physical Dispersion in Surface Wave and Free Oscillation Problems: Review . *Reviews of Geophysics and Space Physics*, 15:105–112, 1977.

[36] J. B. Minster and D. L. Anderson. A Model of Dislocation-Controlled Rheology for the Mantle. *Phils. Trans. R. Soc. London, Ser. A*, 299(1449):319–356, 1981.

[37] S-I. Karato. Importance of anelasticity in the interpretation of seismic tomography. *Geophys. Res. Lett*, 20:1623–1626, 1993.

[38] F. Sohl and T. Spohn. The interior structure of Mars: Implications from SNC meteorites. *J. Geophys. Res.*, 102:1613–1636, 1997.

[39] A. Khan, C. Liebske, A. Rozel, A. Rivoldini, F. Nimmo, J. A. D. Connolly, A. C. Plesa, and D. Giardini. A Geophysical Perspective on the Bulk Composition of Mars. *Journal of Geophysical Research: Planets*, 224(2-4):doi:10.1002/2017JE005371, 2018.

[40] G. Morard, J. Siebert, D. Andrault, N. Guignot, G. Garbarino, F. Guyot, and D. Antonangeli. The Earth's core composition from high pressure density measurements of liquid iron alloys. *Earth Planet. Sci. Lett.*, 373:169–178, 2013.

[41] A. M. Dziewonski and D. L. Anderson. Preliminary reference Earth model. *Phys. Earth. Pl. Int.*, 25:297–356, 1981.

[42] I. Jackson, J. D. Fitz Gerald, U. H. Faul, and B. H. Tan. Grain-size-sensitive seismic wave attenuation in polycrystalline olivine. *J. Geophys. Res.*, 107(B12):doi:10.1029/2001JB001225, 2002.

[43] V. N. Zharkov, T. V. Gudkova, and A. V. Batov. On Estimating the Dissipative Factor of the Martian Interior. *Solar System Research*, 51(6):479–490, 2018.

[44] V. N. Zharkov and T. V. Gudkova. Construction of Martian Interior Model. *Solar System Research*, 39(5):343–373, 2005.

[45] D. L. Anderson and J. W. Given. Absorption-Band Q Model for the Earth. *J. Geophys. Res.*, 87:3893–3904, 1982.

[46] M. Matsui. Molecular dynamics simulation of structures, bulk moduli, and volume thermal expansivities of silicate liquids in the system CaO-MgO-Al_2O_3-SiO_2. *Geophys. Res. Lett*, 23(4):395–398, 1996.

[47] H. Takeuchi and M. Saito. Seismic surfaces waves. In B. A. Bolt, editor, *Methods in Computational Physics*, volume 1, pages 217–294. Academic Press, New York, 1972.

[48] A. S. Konopliv, R. S. Park, and W. M. Folkner. An improved JPL Mars gravity field and orientation from Mars orbiter and lander tracking data. *Icarus*, 274:253–260, 2016.

[49] J. Leconte, G. Chabrier, I. Baraffe, and B. Levrard. Is tidal heating sufficient to explain bloated exoplanets? Consistent calculations accounting for finite initial eccentricity. 516:doi:10.1051/0004–6361/201014337, 2010.

[50] R. Barnes, S. N. Raymond, B. Jackson, and R. Greenberg. Tides and the Evolution of Planetary Habitability. *Astrobiology*, 8(3):557–568, 2008.

[51] D. Baratoux, M. Toplis, M. Monnereau, and O. Gasnault. Thermal history of Mars inferred from orbital geochemistry of volcanic provinces. *Nature*, 472:338–341, 2011.

[52] J. E. P. Connerney, M. H. Acuña, N. F. Ness, T. Spohn, and G. Schubert. Mars crustal magnetism. *Solar System Research*, 11:1–32, 2004.

[53] J. Monteux, A. M. Jellineck, and C. L. Johnson. Why might planets and moons have early dynamos? *Earth Planet. Sci. Lett.*, 310:349–359, 2011.

[54] D. Breuer and T. Spohn. Early plate tectonics versus single-plate tectonics on Mars: Evidence from magnetic field history and crust evolution . *J. Geophys. Res.*, 108:doi:10.1029/2002JE001999, 2003.

[55] S. Clifford and T. J. Parker. The Evolution of the Martian Hydrosphere: Implications for the Fate of a Primordial Ocean and the Current State of the Northern Plains. *Icarus*, 154(1):40–79, 2001.

[56] R. Wordsworth. The climate of early Mars. *Ann. Rev. Earth Planet. Sci.* 44:381–408, 2016.

[57] W. Munk and C. Wunsch. Abyssal recipes II: energetics of tidal and wind mixing. *Deep Sea Research Part I: Oceanographic Research Papers*, 45(12):1977–2010, 1998.

[58] G. D. Egbert and R. D. Ray. Semi-diurnal and diurnal tidal dissipation from TOPEX/Poseidon altimetry. *Geophys. Res. Lett*, 30(17), 2003.

[59] C. Wunsch and R. Ferrari. Vertical mixing, energy, and the general circulation of the oceans. *Ann. Rev. Fluid Mech.*, 36(1):281–314, 2004.

[60] M. H. Carr and J. W. Head. Geologic history of mars. *Earth Planet. Sci. Lett.*, 294(3-4):185–203, 2010.

Table 1: Summary of the symbols and the meaning of the main physical constants and variables used for the modeling of Mars' thermochemical evolution. Brackets indicate an explored range.

Symbol	Meaning	Value	Unit
T_m	Mantle temperature	variable	K
T_c	Core temperature	variable	K
T_{m_0}	Initial Mantle temperature	[1700-2000]	K
T_{c_0}	Initial Core temperature	[1800-2500]	K
T_s	Surface temperature	220	K
T_l	Temperature at base of the lithosphere	variable	K
T_b	Temperature at base of the mantle	variable	K
ρ_m	Mantle density	3500	kg m^{-3}
ρ_c	Core density	7200	kg m^{-3}
ρ_{cr}	Crust density	2900	kg m^{-3}
g	Surface gravity	3.7	m s^{-2}
g_c	Core surface gravity	3.1	m s^{-2}
C_m	Mantle specific heat at constant pressure	1142.0	J kg^{-1} K^{-1}
C_c	Core specific heat at constant pressure	840	J kg^{-1} K^{-1}
C_{cr}	Crust specific heat at constant pressure	1000	J kg^{-1} K^{-1}
k_m	Mantle thermal conductivity	4.0	W m^{-1} K^{-1}
k_{cr}	Crust thermal conductivity	2.5	W m^{-1} K^{-1}
k_c	Core thermal conductivity	40	W m^{-1} K^{-1}
α_m	Silicates thermal expansion coefficient	2.0 10^{-5}	K^{-1}
α_c	Core thermal expansion coefficient	1.5 10^{-5}	K^{-1}
R_p	Mars radius	3.3895 10^6	m
R_m	Radius of Mars' convecting mantle	variable	m
R_c	Mars core radius	1.855 10^6	m
D_l	Stagnant lid thickness	variable	m
D_{cr}	Crust thickness	variable	m
δ_u	Thickness of the core lower thermal boundary	variable	m
δ_c	Thickness of the mantle lower thermal boundary	variable	m
A_m	Convecting mantle surface area	$4\pi R_m^2$	m^2
A_c	Core surface area	$4\pi R_c^2$	m^2
V_m	Volume of the convecting mante	$4\pi R_m^2/3$	m^3
V_c	Volume of the core	$4\pi R_c^2/3$	m^3
St	Stefan number	variable	-
q_m	Heat flow atop of the convecting mantle	variable	W/m^2
q_c	Heat flow at the core-mantle boundary	variable	W/m^2
ϵ_m	Ratio of the convecting mantle temperature and T_m	variable	-
ϵ_c	Ratio of the mean and upper core temperature	1.05	-
u_0	Mantle convective velocity scale	2 10^{-12}	m/s
Λ	Crustal enrichment factor	5	-
H_m	Mantle radioacive heat production rate	variable	W/m^3
H_{cr}	Crust radioacive heat production rate	variable	W/m^3
$H_{0,i}$	Initial heat production rate for ^{238}U,^{235}U, ^{232}Th, ^{40}K	(1.06, 1.95, 0.55, 2.36) 10^{-8}	W m^3
η_m	Mantle viscosity	variable	Pa s
η_c	Mantle viscosity at the core-mantle boundary	variable	Pa s
Ra_c	Critical value of the Rayleigh number	450	-
Rai_c	Local critical Rayleigh number	variable	-
Ra	Thermal Rayleigh number for the convecting mantle	variable	-
Rai	Whole mantle Rayleigh number	variable	-
κ_m	Mantle thermal diffusivity	$k_m/(\rho_m C_m)$	m^2/s
L_m	Mantle latent heat of fusion/crystallization	6 10^5	J/kg

Table 2: Symbols and meaning of the quantities related to Mars' mantle rheology and deformation. Brackets indicate an explored range.

Symbol	Meaning	Value	Unit
R	Gas constant	8.31	J K^{-1} mol^{-1}
E^*	Effective activation energy	[60-350]	kJ/mol
V^*	Effective activation volume	[0-6]	cm^3/mol
$E^*_{\rm disl}$	Activation energy in the dislocation creep regime	$E^*/3.5$	kJ/mol
$V^*_{\rm disl}$	Activation volume in the dislocation creep regime	$V^*/3.5$	cm^3/mol
$P_{\rm ref}$	Reference pressure	3 10^9	Pa
$T_{\rm ref}$	Reference temperature	1600	K
η_0	Reference viscosity	[10^{20}-10^{23}]	Pa s
Q_0	Quality factor constant	variable	-
α_q	Power slope of the quality factor	0.1	-

Table 3: Symbols and meaning of the main physical constants and variables used orbital evolution.

Symbol	Meaning	Value	Unit
k_2	Mars degree 2 Love number	variable	-
k_{2s}	Phobos degree 2 Love number	10^{-7}	-
Q	Mars tidal quality factor	variable	-
Q_s	Phobos tidal quality factor	100	-
M_p	Mars mass	6.41693 10^{23}	kg
M_s	Phobos mass	1.06590 10^{16}	kg
R_s	Phobos radius	11270	m
G	Gravitational constant	6.67408 10^{-11}	$m^3kg^{-1}s^{-2}$
a	Phobos semi-major axis	variable	m
$e_{\rm present}$	Phobos present-day orbital eccentricity	0.0151	-
$a_{\rm present}$	Phobos present-day semi-major axis	2.76 R_p	m
$a_{\rm sync}$	Mars synchronous radius	6.03 R_p	m
n	Mean orbital motion	variable	rad/s
ω_p	Mars rotational frequency	$2\pi/(24.66 \times 3600)$	rad/s